Investigation on the effect of interface properties on compressive failure behavior of 3D woven composites through micromechanics-based multiscale damage model

Zheng, Tao; Guo, Licheng; Sun, Ruijian; Wang, Tongtong; Hong, Changqing; Benedictus, Rinze; Pascoe, John Alan

Important note
To cite this publication, please use the final published version (if applicable).
Please check the document version above.

Check for
updates

Investigation on the effect of interface properties on compressive failure behavior of 3D woven composites through micromechanics-based multiscale damage model

Tao Zheng [a,b], Licheng Guo [a,*], Ruijian Sun [c], Tongtong Wang [a], Changqing Hong [d], Rinze Benedictus [b], John-Alan Pascoe [b,*]

[a] Department of Astronautic Science and Mechanics, Harbin Institute of Technology, Harbin 150001, PR China
[b] Structural Integrity and Composites Group, Faculty of Aerospace Engineering, Delft University of Technology, The Netherlands
[c] Beijing Institute of Astronautical Systems Engineering, Beijing 100076, China
[d] National Key Laboratory of Science and Technology on Advanced Composites in Special Environments, Harbin Institute of Technology, Harbin 150001, China

ARTICLE INFO

ABSTRACT

In this paper, the effect of interface properties on the compressive failure behavior of 3D woven composites (3DWC) is investigated by incorporating a micromechanics-based multiscale damage model (MMDM). The correlation between the mesoscopic stress of yarns and microscopic stress of constituents is established by defining a stress amplification factor. With the microscopic stresses, the fiber breakage and matrix failure can be separately evaluated at the microscale, without assuming the yarns as transversely isotropic homogeneous materials. Especially, the interfacial debonding between yarns and matrix is also a dominant damage mode within 3DWC. Given that there is still a lack of studies on the influence of interfacial properties on the compressive failure behavior of 3DWC, it is meaningful to perform numerical parametric studies to reveal how the interface properties contribute to the damage mechanisms of 3DWC under compressions. The predicted results indicate that with the increase of interface strengths and fracture toughness, the compressive resistance of 3DWC can be significantly improved, resulting in higher strength and failure strain. Additionally, the studied 3DWCs with weak, medium and strong interfaces exhibit different damage development processes.

1. Introduction

Thanks to the superior structural integrity compared to composite laminates, 3D woven composites (3DWC) possess wide applications in aeronautics, aerospace and marine industries [1–4]. 3DWC have many outstanding integrated properties, including exceptional impact resistance, excellent fatigue characteristics and good structural designability [5]. However, the failure behaviors of 3DWC are quite complex due to the complexity of the mesoscopic woven architectures. Generally, the actual damage mechanisms of 3DWC is difficult to determine through experimental characterizations. Although the dominant damage modes can be observed based on the final fracture topography of failed specimens, the damage accumulation process is difficult to capture by experimental detection techniques. In view of this situation, feasible and accurate numerical methods for studying the failure behavior of 3DWC are highly needed to be developed.

Mesoscopic numerical simulations combining a representative volume cell (RVC) have emerged as an useful approach to investigating the damage mechanisms of textile composites [6–10]. Zako et al. [6] employed a RVC model to simulate the failure behaviors of fabric composites. Zeng et al. [7] proposed a user-friendly multiphase RVC to analyze the nonlinear response of 3D braided composites (3DBC). To consider the influence of yarn distortions, Fang et al. [8] divided the octagonal cross-sections of yarns into seven regions, each imposing a different local coordinate system. Zhang et al. [9] then used three unit-cells to reconstruct the skin-core architecture of textile composites. Later, Ge et al. [10] simulated the nonlinear responses of 3DBC using an elastoplastic model, and the various damage modes of yarns were detected by Hashin criteria [11]. The mesoscopic computations assume the tows as a transversely isotropic homogeneous material. However, the above assumption does not seem rigorous enough because the tows consist of fibers and matrix. To judge the microscopic failure, Ha et al.

---

[12] proposed the micromechanics of failure theory (MMF), where a correlation between the mesoscopic stresses of tows and microscopic stresses of constituents was established by introducing a stress amplification factor (SAF). Subsequently, the MMF theory has been employed to predict the damage responses of laminated composites [13–15] and 2D textile composite [16,17]. However, for 3D textile composites, the application of MMF theory is rarely reported.

Apart from matrix failure and the multiple failure modes within the tows, the interfacial debonding between tows and matrix is also a dominant damage mode within 3DWC [18–21]. Thus, the interfacial debonding should also be considered in the numerical simulation of 3DWC. Due to the complex *meso*-woven structure, the interfacial properties inside 3DWC are difficult to directly measure through experiments [22]. But fortunately, the numerical computations can effectively break through this limitation. With the interfacial constitutive model, the interfacial debonding can be precisely predicted. In the absence of experimental data, many scholars have numerically studied the influence of interface property on the failure behaviors of textile composites [23–26]. A parametric study, performed by Fang et al. [23], indicated that interfacial damage resulted in nonlinearity and stiffness reduction of 3DBC, but the tensile failure strengths were not obviously affected. Lu et al. [24] have numerically studied the influences of interface property on the tensile damage mechanisms of 3DBC. It is observed the tensile behaviors were significantly affected by the interfacial strengths. Subsequently, Lu et al. [25] found the tensile ultimate strengths of 3DWC were greatly influenced by the interfacial fracture toughness, but did not increase monotonically with the increasing fracture toughness. Based on a molecular dynamics based interface model, Wang et al. [26] have studied the effects of interfacial friction coefficients on the progressive damage in 3D SiC$_f$/SiC composites under monotonic tensile loadings. Negligible influence of interfacial friction coefficients was found on the failure strengths, and a similar phenomenon was also observed in reference [22]. It is noted that the above studies are all focused on the tensile conditions, while investigations of interfacial properties on the compressive performances of 3DWC are still lacking. Therefore, it is meaningful to conduct numerical parametric studies to reveal how the interface parameters contribute to the effective property and damage developments of 3DWC under compressions.

This work investigates the effects of interfacial parameters on the compressive failure behaviors of 3DWC through a MMDM. The paragraphs of this paper are organized as follows: the microscopic and mesoscopic RVCs are constructed to simulate the multiscale geometry of 3DWC in section 2. To bridge the numerical computations of mesoscale and microscale, a stress transfer process is established based on the SAF of MMF theory. Section 3 presents the micromechanical analyses of micro RVC there were conducted to calculate the SAF. A MMDM is proposed in section 4 to simulate the compressive responses of 3DWC. Section 5 reports on the influences of interfacial property on the compressive performances of 3DWC based on a numerical evaluation.

Section 6 presents the conclusions based on the analyses of the numerical predictions.

2. Geometrical modeling of 3DWC containing interfaces

2.1. Spatial reinforcement of fiber tows

3D woven composites (3DWC) with spatial reinforcement of fiber tows are chosen as the study materials in this work. As displayed in Fig. 1, the 3DWC is composed of three different types of fiber tows and is impregnated by TDE-86 epoxy resin. Weft and warp tow has 12 K-T700 carbon fiber, and binder tow has 3 K-T300 carbon fibers. The global fiber fraction of 3DWC is 50.9 %. The mechanical properties of the fibers and matrix material have been presented in Table 1. The warp tows and weft tows are distributed along two mutually perpendicular directions. The warp layer and weft layer are sequentially stacked in the thickness direction, and they are interlocked by introducing a set of binder tows, which effectively enhances the inter-layer performance of the structure. Specimens of this 3DWC were cut in different directions, and the internal woven structure was then observed by an optical microscope. The binder yarns present regular fluctuations, and the weft and warp yarns also present slight fluctuations caused by the manufacturing process.

2.2. Mesoscopic RVC of 3DWC

The geometric reconstruction of the RVC was performed in the software TexGen by compiling a python script. As shown in Fig. 2, the binder yarns consist of two curved segments (A and B). The segment B is created according to the cross-section shape of weft yarns, and segment A is created by connecting different B segments. The weft yarns are constructed using sinusoidal curves, while the slight fluctuations in the warp yarns are ignored. According to microscopic observation in Fig. 1, the cross-sections of warp and weft yarns can be approximated by elliptical shape, and the cross-section of binder yarns can be approximated by lenticular shape. The woven architecture is periodic in the in-plane directions, and the middle layers occupy the majority of the

Table 1
The material properties of fiber, yarns and matrix.

Fiber [27]	E_{f1} GPa	E_{f2} GPa	G_{f12} GPa	ν_{f12}	ν_{f23}
T700	230.0	18.20	36.62	0.27	0.30
T300	221.0	13.81	9.00	0.20	0.25
Fiber yarns	E_1	E_2	G_{12}	ν_{12}	ν_{23}
Binder (75.0 %)	166.64	9.43	4.74	0.23	0.33
Weft (84.6 %)	195.01	13.22	12.57	0.28	0.38
Warp (87.9 %)	202.50	14.19	16.40	0.28	0.38
Matrix [27]	E_m	ν_m	S_t MPa	S_c MPa	
TDE-86	3.55	0.33	80.0	241.0	
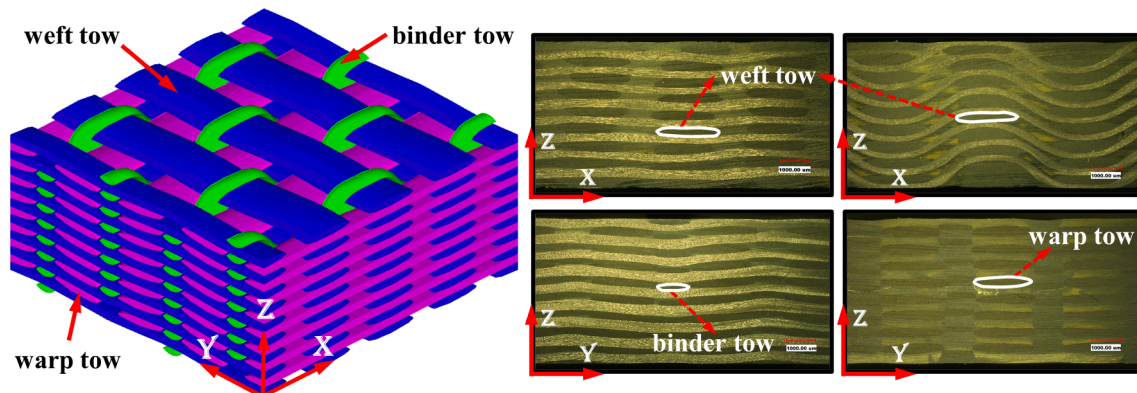
Fig. 1. Spatial reinforcement of fiber tows within 3D woven composites.
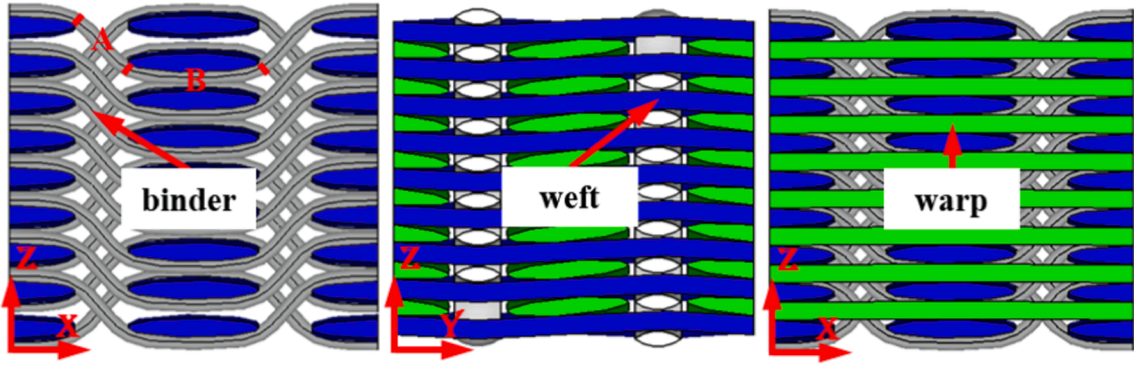
Fig. 2. Geometric models of binder, weft and weft yarns inside 3D woven composites.

structure. To limit the number of elements (and thus the computational cost), a mesoscopic RVC of 3DWC shown in Fig. 3 was extracted to carry out the numerical predictions. Due to the complex geometric structure, the C3D4 element type with better boundary adaptability was adopted to discrete the RVC. The application of 4-noded tetrahedral elements can effectively reduce the computational costs of the numerical parametric study, although this may sacrifice a certain degree of stress accuracy. To enable the applications of periodic boundary condition, it is necessary to ensure the mesh periodicity on the face, edge and vertex boundaries of the RVC [28]. After generating the elements of the RVC, there is a set of smooth boundaries between the tows and matrix, where the elements are connected by common nodes. Based on these common nodes, zero-thickness elements (COH3D6) were created to capture the interfacial debonding.

2.3. Hexagonal micro RVC of tows

The microscale of 3DWC refers to the scale of pure fibers and matrix and is therefore the relevant scale for understanding the damage mechanisms that occur within the tows. A parametric study was performed by Huang et al. [29] to investigate the effects of different microscopic RVCs on the properties of UD composite. The effective properties and stress distributions of different fiber distributions were comprehensively compared. Huang et al. [29] concluded that the properties obtained by hexagonal arrays agree well with those of random arrays. In addition, the hexagonal array can also achieve relatively higher fiber volume fraction within the yarns (up to 90.6 %). Therefore, in this study, the hexagonal micro RVE presented in Fig. 4 was chosen to derive the properties and stress distribution of fiber tows. It is noted that the L and W were set to 1, and H was set to $\sqrt{3}$.

3. Correlation between mesoscale and microscale

3.1. Strain and stress amplification factors (SSAF)

A meso-to-micro stress transfer process is required to bridge the numerical computations of mesoscale and microscale. The correlation between mesoscopic components of yarns ($\overline{\sigma}_f$, $\overline{\varepsilon}_f$) and microscopic components within constituents (σ_{ff}, σ_{fm}, ε_{ff}, ε_{fm}) was established by defining a strain and stress amplification factor (SSAF) as follows:

$$\begin{cases} \boldsymbol{\sigma}_{ff} = \boldsymbol{M}_{f\sigma}\overline{\boldsymbol{\sigma}}_f, \ \boldsymbol{\sigma}_{fm} = \boldsymbol{M}_{m\sigma}\overline{\boldsymbol{\sigma}}_f \\ \boldsymbol{\varepsilon}_{ff} = \boldsymbol{M}_{f\varepsilon}\overline{\boldsymbol{\varepsilon}}_f, \ \boldsymbol{\varepsilon}_{fm} = \boldsymbol{M}_{m\varepsilon}\overline{\boldsymbol{\varepsilon}}_f \end{cases} \tag{1}$$

where $\boldsymbol{M}_{f\sigma}$ and $\boldsymbol{M}_{m\sigma}$ denote the stress SAF, and $\boldsymbol{M}_{f\varepsilon}$ and $\boldsymbol{M}_{m\varepsilon}$ are the strain SAF. SSAF are 6×6 matrices, and the general expression of strain SAF can be determined by utilizing the following basic understandings [30]: the longitudinal micro and mesoscopic strains of yarns are equivalent; the micro transverse strains (ε_{22}, ε_{33}) and shear strain (γ_{23}) are dominated by their mesoscopic counterparts; the micro shear strains (γ_{12}, γ_{13}) are only determined by their mesoscopic counterparts. In summary, the complete form of the strain relationships in Eq. (1) can be expanded as:

$$\begin{pmatrix} \varepsilon_{11} \\ \varepsilon_{22} \\ \varepsilon_{33} \\ \gamma_{12} \\ \gamma_{13} \\ \gamma_{23} \end{pmatrix}_{\substack{ff \\ fm}} = \begin{bmatrix} 1 & 0 & 0 & 0 & 0 & 0 \\ M_{\varepsilon,21} & M_{\varepsilon,22} & M_{\varepsilon,23} & 0 & 0 & M_{\varepsilon,26} \\ M_{\varepsilon,31} & M_{\varepsilon,32} & M_{\varepsilon,33} & 0 & 0 & M_{\varepsilon,36} \\ 0 & 0 & 0 & M_{\varepsilon,44} & M_{\varepsilon,45} & 0 \\ 0 & 0 & 0 & M_{\varepsilon,54} & M_{\varepsilon,55} & 0 \\ M_{\varepsilon,61} & M_{\varepsilon,62} & M_{\varepsilon,63} & 0 & 0 & M_{\varepsilon,66} \end{bmatrix} \begin{pmatrix} \overline{\varepsilon}_{f11} \\ \overline{\varepsilon}_{f22} \\ \overline{\varepsilon}_{f33} \\ \overline{\gamma}_{f12} \\ \overline{\gamma}_{f13} \\ \overline{\gamma}_{f23} \end{pmatrix} \tag{2}$$

Subsequently, the expression of stress SAF can be obtained by the following relation with the strain SAF [30]:

$$\boldsymbol{M}_{f\sigma} = \boldsymbol{C}_f \boldsymbol{M}_{f\varepsilon} \overline{\boldsymbol{C}}_f^{-1}; \ \boldsymbol{M}_{m\sigma} = \boldsymbol{C}_m \boldsymbol{M}_{m\varepsilon} \overline{\boldsymbol{C}}_f^{-1} \tag{3}$$

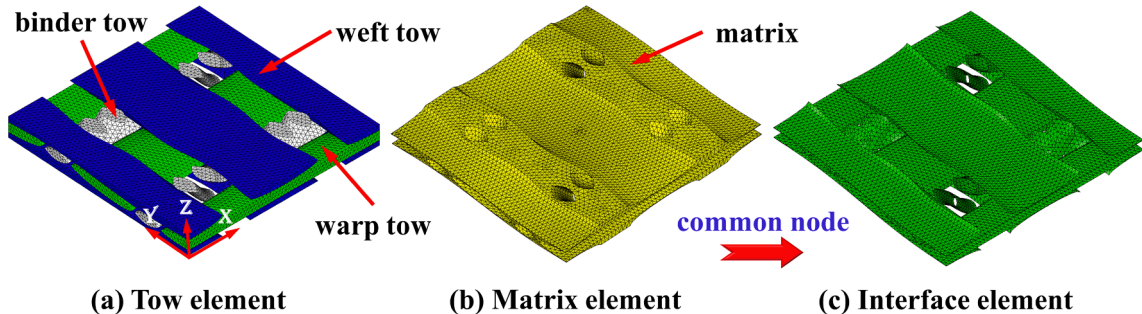**(a) Tow element**   **(b) Matrix element**   **(c) Interface element**

Fig. 3. Mesoscopic representative volume cell of 3DWC containing interface.
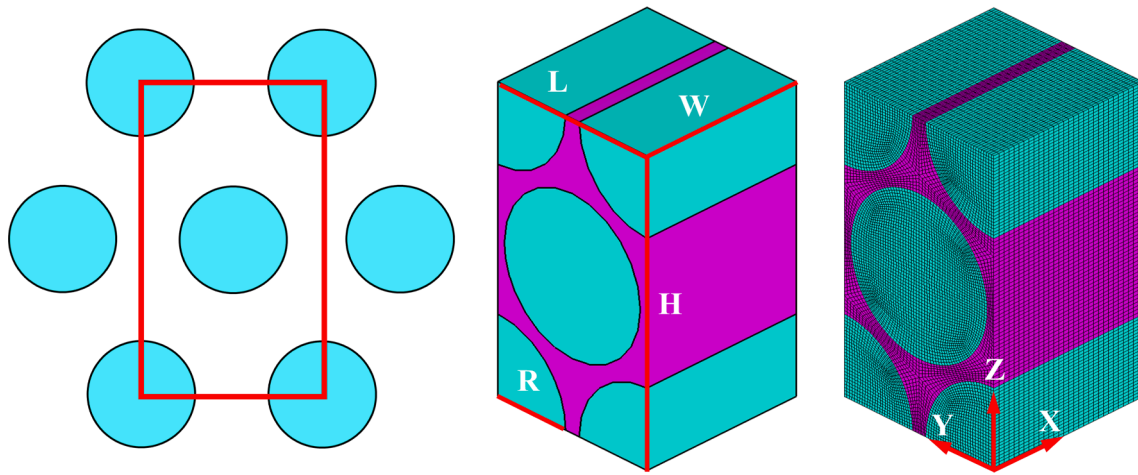
Fig. 4. Hexagonal micro representative volume cell of fiber tows.

where $\boldsymbol{C}_m$ and $\boldsymbol{C}_f$ denote the stiffness matrices of pure matrix and fibers, respectively. $\overline{\boldsymbol{C}}_f$ denotes the stiffness matrix of yarns. Eq. (3) can be further expanded as:

3.2. Calculation of SSAF

The stress distributions of microscopic RVC are not uniform, which means that there are different SSAF at different locations. It is necessary

$$
\boldsymbol{M}_\sigma = \begin{bmatrix} C_{11} & C_{12} & C_{13} & 0 & 0 & 0 \\ C_{21} & C_{22} & C_{23} & 0 & 0 & 0 \\ C_{31} & C_{32} & C_{33} & 0 & 0 & 0 \\ 0 & 0 & 0 & C_{44} & 0 & 0 \\ 0 & 0 & 0 & 0 & C_{55} & 0 \\ 0 & 0 & 0 & 0 & 0 & C_{66} \end{bmatrix} \boldsymbol{M}_\varepsilon \begin{bmatrix} \overline{C}_{f,11} & \overline{C}_{f,12} & \overline{C}_{f,13} & 0 & 0 & 0 \\ \overline{C}_{f,21} & \overline{C}_{f,22} & \overline{C}_{f,23} & 0 & 0 & 0 \\ \overline{C}_{f,31} & \overline{C}_{f,32} & \overline{C}_{f,33} & 0 & 0 & 0 \\ 0 & 0 & 0 & \overline{C}_{f,44} & 0 & 0 \\ 0 & 0 & 0 & 0 & \overline{C}_{f,55} & 0 \\ 0 & 0 & 0 & 0 & 0 & \overline{C}_{f,66} \end{bmatrix}^{-1}
\tag{4}
$$

As a result, the general expression of the stress SAF can be written as:

$$
\boldsymbol{M}_\sigma = \begin{bmatrix} M_{\sigma,11} & M_{\sigma,12} & M_{\sigma,13} & 0 & 0 & M_{\sigma,16} \\ M_{\sigma,21} & M_{\sigma,22} & M_{\sigma,23} & 0 & 0 & M_{\sigma,26} \\ M_{\sigma,31} & M_{\sigma,32} & M_{\sigma,33} & 0 & 0 & M_{\sigma,36} \\ 0 & 0 & 0 & M_{\sigma,44} & M_{\sigma,45} & 0 \\ 0 & 0 & 0 & M_{\sigma,54} & M_{\sigma,55} & 0 \\ M_{\sigma,61} & M_{\sigma,62} & M_{\sigma,63} & 0 & 0 & M_{\sigma,66} \end{bmatrix}
\tag{5}
$$

to conduct micromechanics calculations to calculate the SSAF. To avoid large computation costs, multiple key elements need to be chosen as representative. There are total 56 matrix and 50 fiber key elements as indicated in Fig. 5. In the aspect of SSAF calculations, six independent unit loadings are separately loaded to RVC. For instance, when applying the unit loading $\overline{\boldsymbol{\sigma}}_f = [1, 0, 0, 0, 0, 0]^T$, the stress components of key elements can be extracted, then the first column of $\boldsymbol{M}_{m\sigma}$ and $\boldsymbol{M}_{f\sigma}$ are obtained. The remaining columns of the SSAF can be calculated in the

(a) Fiber key element **(b) Matrix model A** **(c) Matrix model B**
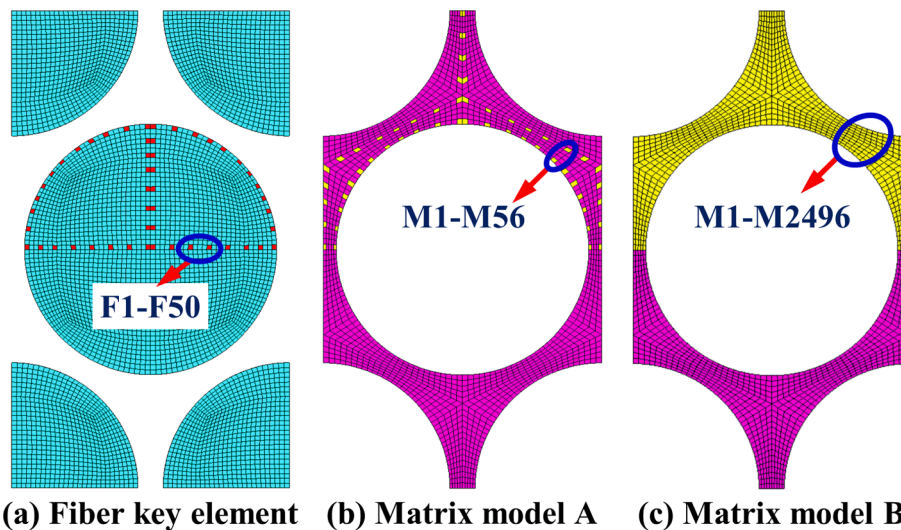
Fig. 5. Key elements within micro RVC: (a) fiber key elements (F_1-F_{50}); (b) matrix key elements of model A (M_1-M_{56}); (c) matrix key elements of model B (M_1-M_{2496}).

same way by sequentially setting the related stress to one and other stresses to zero. In later **section 5.1**, a parametric study will be presented to verify that the number of key elements is sufficient to capture the stress concentrations within the micro RVC, and the SSAF calculated by half of all matrix elements (**model B**) will be compared with those calculated by only 56 key elements (**model A**).

4. Micromechanics-based multiscale damage model

4.1. Matrix failure and damage evolution

The matrix outside the yarns can be considered isotropic. Under complex loads, the matrix failure is dominated by the first stress invariant and von Mises stress. In this paper, the following failure criterion proposed by Raghava [31] is applied to determine the matrix failure:

$$\phi_m = [(S_c - S_t)I_{1,m} + \sigma_{VM,m}^2]/(S_t S_c) = 1 \tag{6}$$

where S_t and S_c denote the tensile and compressive strengths, respectively. The above criterion can be simplified to a Stassi's equivalent stress [32]:

$$\sigma_{eq,m} = \left[\left((S_c - S_t)I_{1,m} + \sqrt{4S_t S_c \sigma_{VM,m}^2 + (S_c - S_t)^2 I_{1,m}^2} \right) \middle/ (2S_c) \right] \tag{7}$$

Huang et al. [13] pointed out that the matrix damage will be initiated when the equivalent stress equals the matrix tensile strength. There is a corresponding equivalent displacement:

$$X_{eq,m} = l_{c,m} \frac{(S_c - S_t)J_{1,m} + \sqrt{(S_c - S_t)^2 J_{1,m}^2 + \left(\frac{2-4\nu_m}{1+\nu_m}\right)^2 S_t S_c \varepsilon_{VM,m}^2}}{2S_c(1-2\nu_m)} \tag{8}$$

where ν_m, $J_{1,m}$ and $\varepsilon_{VM,m}$ denote the Poisson's ratio, first strain invariant and von Mises strain, respectively. After the matrix damage is triggered, the properties of the matrix will gradually degrade. To facilitate numerical implementation, the damage variable of matrix can be determined by a linear evolution model:

$$d_m = \frac{X_{eq,m}^f(X_{eq,m} - X_{eq,m}^i)}{X_{eq,m}(X_{eq,m}^f - X_{eq,m}^i)}, \quad X_{eq,m}^i \leqslant X_{eq,m} \leqslant X_{eq,m}^f \tag{9}$$

As displayed in Fig. 6, $X_{eq,m}^i = l_{c,m} S_t / E_m$ and $X_{eq,m}^f = 2G_{C,m}/S_t$ [33] denote the equivalent displacements associated with the initial and final failure points of matrix, respectively. Here, $G_{C,m}$ represents the fracture toughness and E_m is the stiffness constant. The constitutive equation with damage variable of matrix is described by $\sigma_m = (1-d_m)C_m\varepsilon_m$.

4.2. Damage model for fiber yarns

Based on the SSAF, the yarns' stresses can be transferred to the fiber filaments and the matrix. With the microscopic stresses of constituents, the fiber fracture and matrix failure can be separately judged at the microscale. According to experimental observations [18], fiber kinking and transverse cracks are the two primary damage modes of fiber bundles under compressive loading. Because these two damage modes are actually caused by micro matrix failure, only the matrix stress needs to be obtained when judging damage initiations. The transverse inter-fiber failure can be determined through the following equation:

$$\phi_{fm} = \max \left[\frac{(S_c - S_t)I_{1,fm}^{(N)} + \sqrt{4S_t S_c \left[\sigma_{VM,fm}^{(N)}\right]^2 + (S_c - S_t)^2 \left[I_{1,fm}^{(N)}\right]^2}}{2S_c S_t} \right], N$$
$$\in [1, \ 56] \tag{10}$$

where $I_{1,fm}^{(N)}$ and $\sigma_{VM,fm}^{(N)}$ are calculated from the microscopic matrix stresses ($\sigma_{fm}^{(N)}$). As mentioned in **section 3**, $\sigma_{fm}^{(N)}$ can be obtained by transforming the mesoscopic stresses ($\overline{\sigma}_f$) in the local system of tows ($1-2-3$) as shown in Fig. 7:

$$\sigma_{fm}^{(N)} = M_{m\sigma}^{(N)} \overline{\sigma}_f, N \in [1, \ 56] \tag{11}$$

In this paper, a combination of 3D kinking model [34] and SSAF is used to determine the fiber kinking. The kinking criterion is the same as **Eq. (10)**, but the stresses $I_{1,fm}^{(N)}$ and $\sigma_{VM,fm}^{(N)}$ need to be replaced with the stresses $I_{1,fm}^{m(N)}$ and $\sigma_{VM,fm}^{m(N)}$, which are calculated from the microscopic matrix stresses ($\sigma_{fm}^{m(N)}$) in the misalignment system ($1^m - 2^m - 3^m$). The stress $\sigma_{fm}^{m(N)}$ can be obtained based on SSAF:

$$\sigma_{fm}^{m(N)} = M_{m\sigma}^{(N)} \overline{\sigma}_f^m, N \in [1, \ 56] \tag{12}$$

where the mesoscopic stress $\overline{\sigma}_f^m$ in $1^m - 2^m - 3^m$ system is calculated from the stress $\overline{\sigma}_f^k$ in kinking system ($1^k - 2^k - 3^k$) as follows:

$$\begin{cases} \overline{\sigma}_{f11}^m = (\overline{\sigma}_{f11}^k - \overline{\sigma}_{f22}^k)\cos^2\phi + \overline{\sigma}_{f22}^k + \overline{\tau}_{f12}^k \sin\theta\cos\theta \\ \overline{\sigma}_{f22}^m = (\overline{\sigma}_{f22}^k - \overline{\sigma}_{f11}^k)\cos^2\phi + \overline{\sigma}_{f11}^k - \overline{\tau}_{f12}^k \sin\theta\cos\theta \\ \overline{\sigma}_{f33}^m = \overline{\sigma}_{f33}^k \\ \overline{\tau}_{f12}^m = 2(\overline{\sigma}_{f22}^k - \overline{\sigma}_{f11}^k)\sin\theta\cos\theta + \overline{\tau}_{f12}^k \cos2\phi \\ \overline{\tau}_{f13}^m = \overline{\tau}_{f13}^k \cos\phi + \overline{\tau}_{f23}^k \sin\phi \\ \overline{\tau}_{f23}^m = -\overline{\tau}_{f13}^k \sin\phi + \overline{\tau}_{f23}^k \cos\phi \end{cases} \tag{13}$$
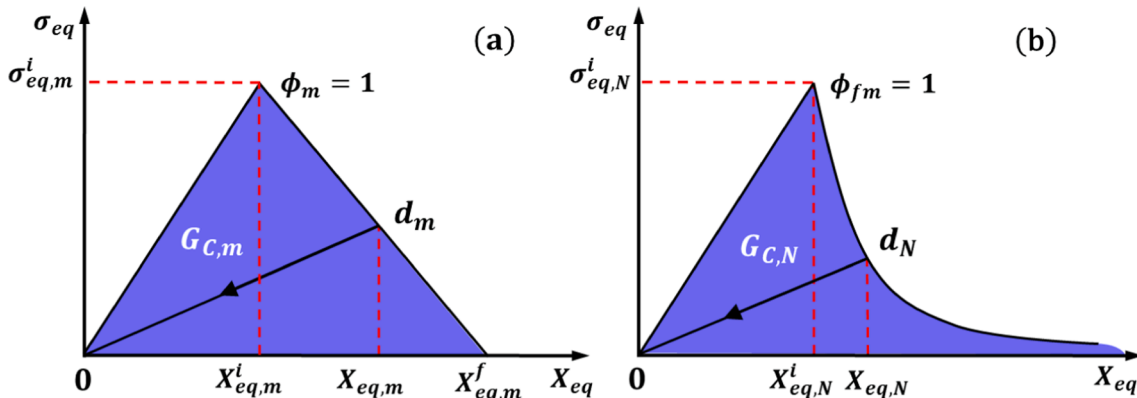

Fig. 6. Damage evolution models for (a) matrix and (b) fiber tows.

The stress $\overline{\sigma}_f^k$ in $1^k - 2^k - 3^k$ system and $\overline{\sigma}_f$ in $1 - 2 - 3$ system can be converted by the following formulas:

$$
\begin{cases}
\overline{\sigma}_{f11}^k = \overline{\sigma}_{f11} \\
\overline{\sigma}_{f22}^k = (\overline{\sigma}_{22} - \overline{\sigma}_{33})\cos^2\theta + \overline{\sigma}_{33} + \overline{\tau}_{23}\sin\theta\cos\theta \\
\overline{\sigma}_{f33}^k = (\overline{\sigma}_{33} - \overline{\sigma}_{22})\cos^2\theta + \overline{\sigma}_{22} - \overline{\tau}_{23}\sin\theta\cos\theta \\
\overline{\tau}_{f12}^k = \overline{\tau}_{f12}\cos\theta + \overline{\tau}_{f13}\sin\theta \\
\overline{\tau}_{f13}^k = -\overline{\tau}_{f12}\sin\theta + \overline{\tau}_{f13}\cos\theta \\
\overline{\tau}_{f23}^k = 2(\overline{\sigma}_{f33} - \overline{\sigma}_{f22})\sin\theta\cos\theta + \overline{\tau}_{f23}\cos2\theta
\end{cases}
\tag{14}
$$

$$
\begin{bmatrix}
C_{11}(1-d_1) & C_{12}(1-d_1)(1-d_2) & C_{13}(1-d_1)(1-d_3) & & & \\
& C_{22}(1-d_2) & C_{23}(1-d_2)(1-d_3) & & 0 & \\
& & C_{33}(1-d_3) & & & \\
& & & C_{44}(1-d_1)(1-d_2) & & \\
& SYM & & & C_{55}(1-d_1)(1-d_3) & \\
& & & & & C_{66}(1-d_2)(1-d_3)
\end{bmatrix}
\tag{19}
$$

The relationships between the three coordinate systems in Fig. 7 are described by θ and ϕ, which are related to the mesoscopic stresses and an initial misalignment angle ϕ_0.

$$
\theta = \frac{1}{2}tan^{-1}\left(\frac{2\overline{\tau}_{f23}}{\overline{\sigma}_{f22} - \overline{\sigma}_{f33}}\right), \quad \phi = \frac{|\overline{\tau}_{f12}^k| + \phi_0 G_{f12}}{G_{f12} + \overline{\sigma}_{f11}^k - \overline{\sigma}_{f22}^k}
\tag{15}
$$

To characterize the brittle fractures of yarns, the post-failure behavior of yarns is described by an exponential evolution model [35] presented in Fig. 6(b). The damage variables are defined using fracture toughness $G_{C,N}$ and equivalent displacement as follows:

$$
d_N = 1 - \frac{X_{eq,N}^i}{X_{eq,N}}\exp\left[\left(1 - \frac{X_{eq,N}}{X_{eq,N}^i}\right)\frac{2\sigma_{eq,N}^i X_{eq,N}^i}{(2G_{C,N} - \sigma_{eq,N}^i X_{eq,N}^i)}\right], \quad N
$$
$$
= \begin{Bmatrix} kink, f2t, f2c \\ f3t, f3c \end{Bmatrix}
\tag{16}
$$

where the equivalent stresses $\sigma_{eq,N}$ and displacements $X_{eq,N}$ are summarized in Table 2. In particular, the initial equivalent stress and displacement of yarns are determined as follows:
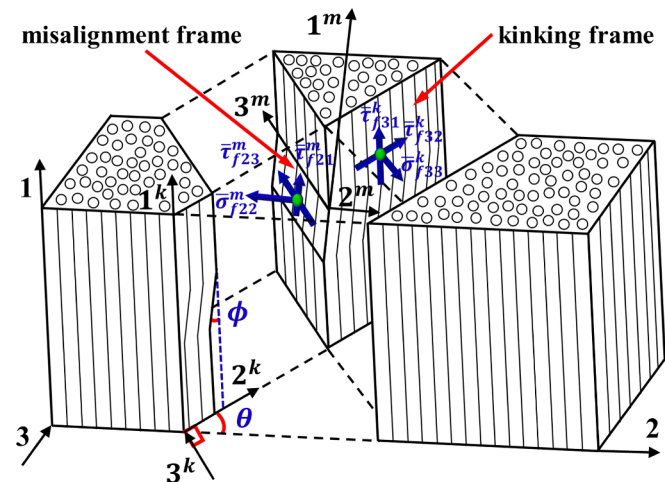

Fig. 7. Misalignment and kinking systems of fiber tows under longitudinal compression [33].

$$
\begin{cases}
\sigma_{eq,N}^i = \sigma_{eq,N}/\phi_{fm,kink}; \ X_{eq,N}^i = X_{eq,N}/\phi_{fm,kink}, \ N = \{kink\} \\
\sigma_{eq,N}^i = \sigma_{eq,N}/\phi_{fm,iff}; \ X_{eq,N}^i = X_{eq,N}/\phi_{fm,iff}, \ N = \{f2t,f2c,f3t,f3c\}
\end{cases}
\tag{17}
$$

After calculating the d_N, the following constitutive relations [36,37] are employed to characterize the damage in fiber tows:

$$
\overline{\sigma}_f = \overline{C}_f(d)\overline{\varepsilon}_f
\tag{18}
$$

where $\overline{C}_f(d)$ denotes the damage constitutive matrix and can be expanded as:

where the damage variables are obtained by the following equations:

$$
d_1 = d_{kink}; \ d_2 = \max(d_{f2t}, d_{f2c}); \ d_3 = \max(d_{f3t}, d_{f3c})
\tag{20}
$$

The numerical implementation of the micromechanics-based damage model was accomplished by writing a user-defined subroutine UMAT, which was integrated into the ABAQUS/Standard.

4.3. Cohesive zone model for interfaces

The cohesive zone model [40,41] is applied to simulate the interfacial debonding between yarns and matrix. The traction-separation relationships of interfaces with damage are:

$$
\sigma_N = (1-d)K_N\delta_N, \ N = (n, \ s, \ t)
\tag{21}
$$

where σ_n, σ_s, and σ_t are the tractions corresponding to the normal and shear directions, respectively, and δ_N are their displacement counterparts. The onset of interface debonding can be determined by the following stress criterion:

$$
(\langle\sigma_n\rangle/\sigma_{n,\max})^2 + (\sigma_s/\sigma_{s,\max})^2 + (\sigma_t/\sigma_{t,\max})^2 = 1
\tag{22}
$$

where $\sigma_{n,\max}$, $\sigma_{s,\max}$, $\sigma_{t,\max}$ are the tensile and shear strengths. It can be seen that compressive normal stress does not contribute to the damage of the interfaces. After the damage initiation, the linear softening law is adopted to reduce the interface stiffness based on the dissipated energy during the damage process:

$$
G_C = 1/\sqrt{(m_1/G_{n,C})^2 + (m_2/G_{s,C})^2 + (m_3/G_{t,C})^2}
$$
$$
m_1 = \frac{G_n}{G_n + G_s + G_t}, m_2 = \frac{G_s}{G_n + G_s + G_t}, m_3 = \frac{G_t}{G_n + G_s + G_t}
\tag{23}
$$

where G_C denotes the mixed-mode fracture energy. G_n, G_s and G_t are the works done in three directions, and $G_{n,C}$, $G_{s,C}$ and $G_{t,C}$ are their corresponding critical fracture energies. Considering that no precise interfacial properties are available, a reasonable discussion range of strength and fracture toughness needs to be determined. It is noted that the interface stiffness needs to be large enough to ensure the displacement continuities [42], so the stiffness K_N is set to 10^8 MPa/mm in this paper. According to the literature [43–46], the interfacial strength mostly varies from 60 to 90 MPa, and the fracture toughness ranges from 0.1 to 0.5 N/mm. To facilitate the parametric analysis in the later section, the strength and fracture toughness in the normal and shear directions are assumed to be the same. Therefore, the discussion ranges for strength

Table 2

The $X_{eq,N}$, $\sigma_{eq,N}$ and fracture toughness related to different damage modes.

Damage modes	$X_{eq,N}$	$\sigma_{eq,N}$	$G_{C,N}$ N/mm [38,39] T700-12 K/T300-3 K
$kink, \overline{\sigma}_{f11} < 0$	$l_c\langle - \overline{\varepsilon}_{f11}\rangle^*$	$l_c\langle - \overline{\varepsilon}_{f11}\rangle\langle - \overline{\sigma}_{f11}\rangle/X_{eq,kink}$	79.90/76.63
$f2t, \overline{\sigma}_{f22}\geqslant 0$	$l_c\sqrt{\langle\overline{\varepsilon}_{f22}\rangle^2 + \overline{\gamma}^2_{f21} + \overline{\gamma}^2_{f23}}$	$l_c(\overline{\sigma}_{f22}\langle\overline{\varepsilon}_{f22}\rangle + \overline{\tau}_{f21}\overline{\gamma}_{f21} + \overline{\tau}_{f23}\overline{\gamma}_{f23})/X_{eq,f2t}$	0.46/0.22
$f2c, \overline{\sigma}_{f22} < 0$	$l_c\sqrt{\langle - \overline{\varepsilon}_{f22}\rangle^2 + \overline{\gamma}^2_{f21} + \overline{\gamma}^2_{f23}}$	$l_c(-\overline{\sigma}_{f22}\langle - \overline{\varepsilon}_{f22}\rangle + \overline{\tau}_{f21}\overline{\gamma}_{f21} + \overline{\tau}_{f23}\overline{\gamma}_{f23})/X_{eq,f2c}$	1.38/0.76
$f3t, \overline{\sigma}_{f33}\geqslant 0$	$l_c\sqrt{\langle\overline{\varepsilon}_{f33}\rangle^2 + \overline{\gamma}^2_{f31} + \overline{\gamma}^2_{f32}}$	$l_c(\overline{\sigma}_{f33}\langle\overline{\varepsilon}_{f33}\rangle + \overline{\tau}_{f31}\overline{\gamma}_{f31} + \overline{\tau}_{f32}\overline{\gamma}_{f32})/X_{eq,f3t}$	0.46/0.22
$f3c, \overline{\sigma}_{f33} < 0$	$l_c\sqrt{\langle - \overline{\varepsilon}_{f33}\rangle^2 + \overline{\gamma}^2_{f31} + \overline{\gamma}^2_{f32}}$	$l_c(-\overline{\sigma}_{f33}\langle - \overline{\varepsilon}_{f33}\rangle + \overline{\tau}_{f31}\overline{\gamma}_{f31} + \overline{\tau}_{f32}\overline{\gamma}_{f32})/X_{eq,f3c}$	1.38/0.76

$*\langle a\rangle = (a + |a|)/2.0.$
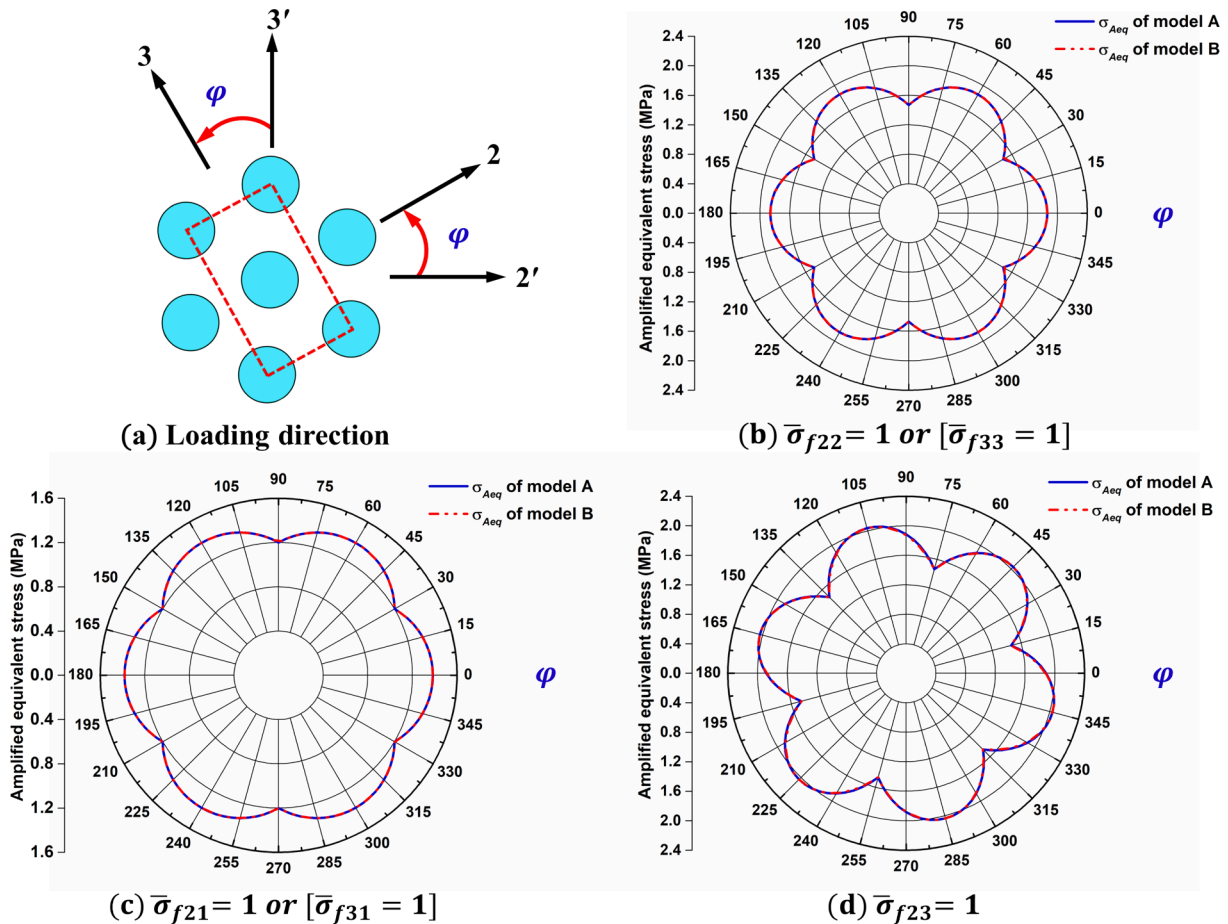
Fig. 8. The amplified equivalent stress σ_{Aeq} of matrix obtained by 56 and 2496 key elements.

$\sigma_{N,max}$ and fracture toughness $G_{N,C}$ of interfaces were set to [10, 120] MPa and [0.1, 0.5] N/mm, respectively.

5. Results and discussion

5.1. Parametric study of key elements

A parametric study was conducted to decide the number of key elements to use in calculating the SAF. 2496 elements of matrix were chosen to calculate the stress amplification factor (SAF), which were then compared with the SAF obtained by only 56 key elements. The amplified equivalent stresses σ_{Aeq} in matrix with loading direction φ are displayed in Fig. 8. It is noted that the larger the σ_{Aeq}, the larger the stress amplification. It can be seen that σ_{Aeq} exhibits slight changes with φ, showing a periodic $60°$ pattern due to the hexagonal fiber distribution.

The amplified equivalent stresses of the matrix obtained when using 56 or 2496 key elements are almost the same, which verifies that 56 elements are sufficient to capture the stress concentration within the matrix. For the fibres, the longitudinal stress of fibers at the microscale (σ_{f11}) is mainly dominated by the axial stress of the yarns ($\overline{\sigma}_{f11}$), and other stress components contribute very little to σ_{f11}. Moreover, the stress distributions within the fiber of micro RVC in the case of $\overline{\sigma}_{f11} = 1$ are uniform, as illustrated in Fig. 9. Therefore, 50 key elements are enough to calculate accurate SAF for the fibres.

5.2. Stress–strain curves with different interface parameters

Fig. 10 displays the experimental and predicted compressive stress–strain curves of 3DWC with different interfacial strengths and fracture toughness. In Fig. 10(a), the interfacial strength varies from 10
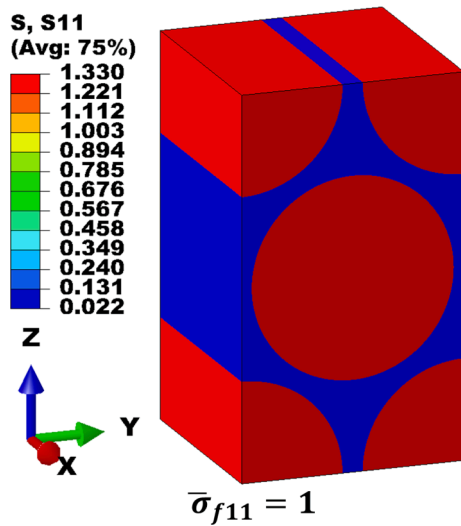
Fig. 9. Stress distribution within micro RVC in the longitudinal case of $\overline{\sigma}_{f11} = 1$.

to 120 MPa, while the fracture toughness remains unchanged at 1 N/ mm. It can be seen that the change in interface strengths has no effect on the initial stiffness of 3DWC, but has a significant effect on the calculated strengths and failure strains. With the increase of interfacial strengths, the compressive resistance of 3DWC is significantly improved, resulting in higher strength and failure strain. However, the predicted strength of 3DWC does not increase continuously. After the interface strength exceeds 80 MPa, the strength of 3DWC will no longer increase, but remains constant. This implies that for interface strengths above 80 MPa, interfacial failure is no longer the critical damage mode.

When the interfacial strength is low, the stress–strain curve deviates from the straight line earlier and exhibits some slight nonlinearity. The average strengths and failure strains obtained from experiments [32] are 495.47 MPa and 1.01 %, respectively. The predicted curves with the interfacial strength in the interval of [30, 60] MPa agree well with the experimental curves. Moreover, the effects of fracture toughness on the predicted strength of 3DWC can be clearly seen from Fig. 10(b). Overall, higher interfacial fracture toughness results in higher strength, as high fracture toughness tends to further enhance the compressive stability of 3DWC. Notably, outside the interfacial strength interval of 30 to 80 MPa, the increase in fracture toughness has almost no effect on the predicted strength. This is due to the fact that for interface strengths below 30 MPa the interface debonding spreads too quickly due to the weak interface, while for strengths above 80 MPa the interface debonding is rarely triggered.

5.3. Effect of interface properties on damage development

The damage development curves corresponding to different damage modes of 3DWC with different interface properties have been presented in Fig. 11. The damage fraction is the ratio of damaged elements to all elements of related constituents. The kink damage fraction, transverse damage fraction and matrix damage fraction have a good correlation with their stress–strain curves. When the interface strength is low, the interfacial debonding occurs very early and propagates rapidly, and finally almost all interface elements fail. The interfacial debonding leads to a decrease in the stress transfer capacity between fiber bundles and matrix, which makes the transverse inter-fiber failure and matrix failure more difficult to accumulate as depicted in Fig. 11(b) and Fig. 11(c). However, due to the lack of support from surrounding components, the longitudinal warp tows are more prone to kinking failure under compressive loading, which results in lower strengths of 3DWC with weak interfaces. To illustrate this intuitively, three different interface strengths are chosen as typical cases as shown in Fig. 12, where the stress contours and the interfacial debonding contours (SDEG) are all taken from the global compressive stress of −200 MPa. Under the same compressive load, the 10 MPa interfaces are seriously damaged, while the 40 MPa interfaces are only slightly damaged, and the 100 MPa interfaces are not damaged. Although all the longitudinal stress distributions of warp tows are close, the shear stress concentration of warp tows with 10 MPa interface is more severe (35.7 > 29.0), which leads to earlier occurrence of fiber kinking. Therefore, the damage process of 3DWC with weak interface is: first interfacial debonding, then shear stress concentration of longitudinal tows, and finally fiber kinking failure.

As shown in Fig. 12, the stress distributions with the interface strengths of 40 and 100 MPa are the same at the initial loading stage since almost no interface debonding occurs. It is necessary to compare the subsequent damage process of 3DWC with the above two interface strengths. To clearly visualize the damage process, the fiber kinking contours and interfacial debonding contours of 3DWC with 40 MPa and 100 MPa interfaces under different global compressive stresses are displayed in Fig. 13 and Fig. 14, respectively. The initial locations of the kinking failure and the global compressive stresses are almost the same for the two interface strengths. In contrast to the 10 MPa interface strength, this initial fiber kinking is 'unassisted' by interfacial debonding. For the 40 MPa interface strength, as the global compressive stress increases, the interfaces near the warp kinking area gradually fail, and the interfacial debonding in turn further accelerates the kinking development. From Fig. 13, it can be seen that the kinking area and interfacial debonding area near the warp tows have a good consistency. However, this consistency cannot be observed in the 100 MPa interfaces as shown
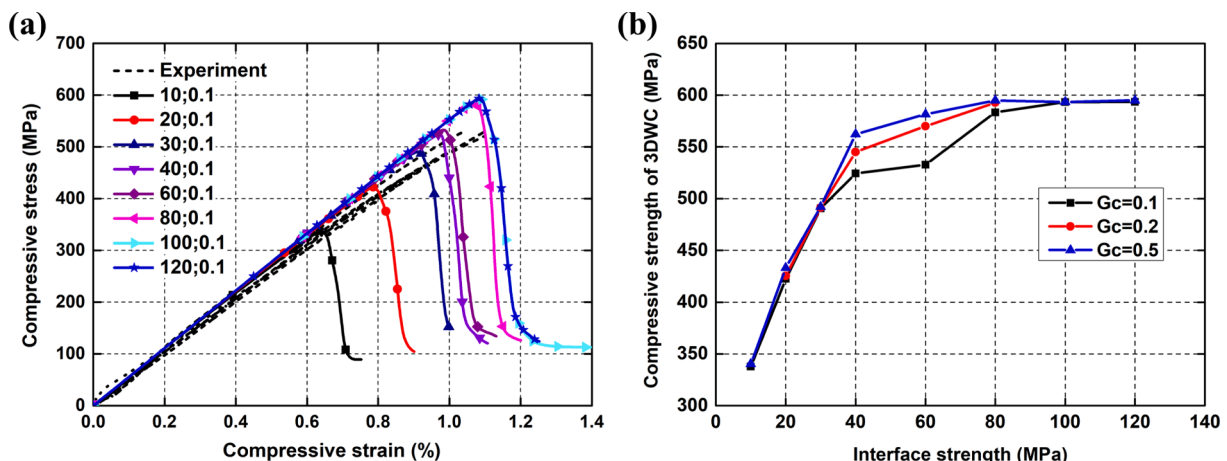

Fig. 10. Predicted stress–strain curves of 3DWC with different interfacial strengths and fracture toughness.
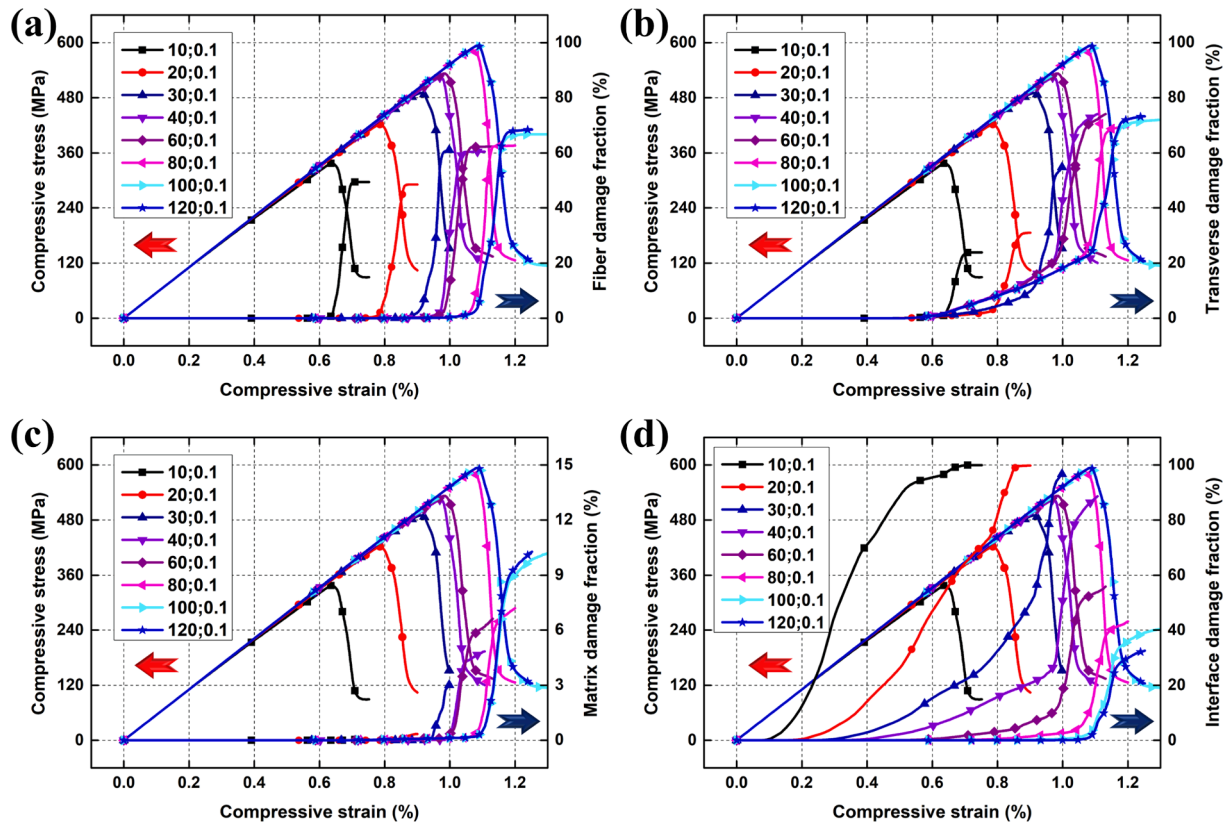
Fig. 11. Effects of interfacial strengths on the damage development curves of 3DWC under compression: (a) fiber kinking, (b) transverse inter-fiber failure, (c) matrix failure, (d) interfacial debonding.
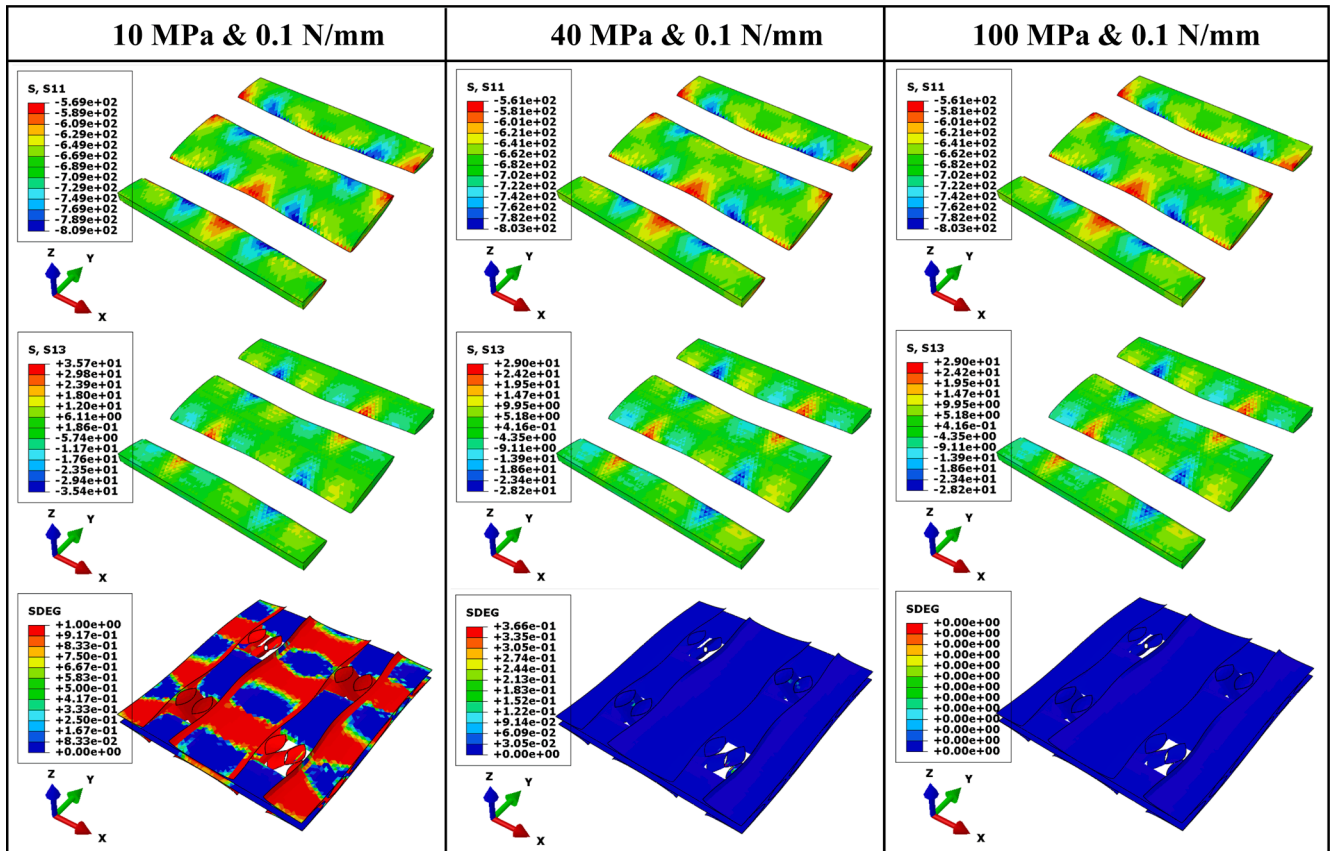

Fig. 12. Stress contours and interfacial debonding contours of 3DWC with three different interface strengths under global compressive stress of −200 MPa.
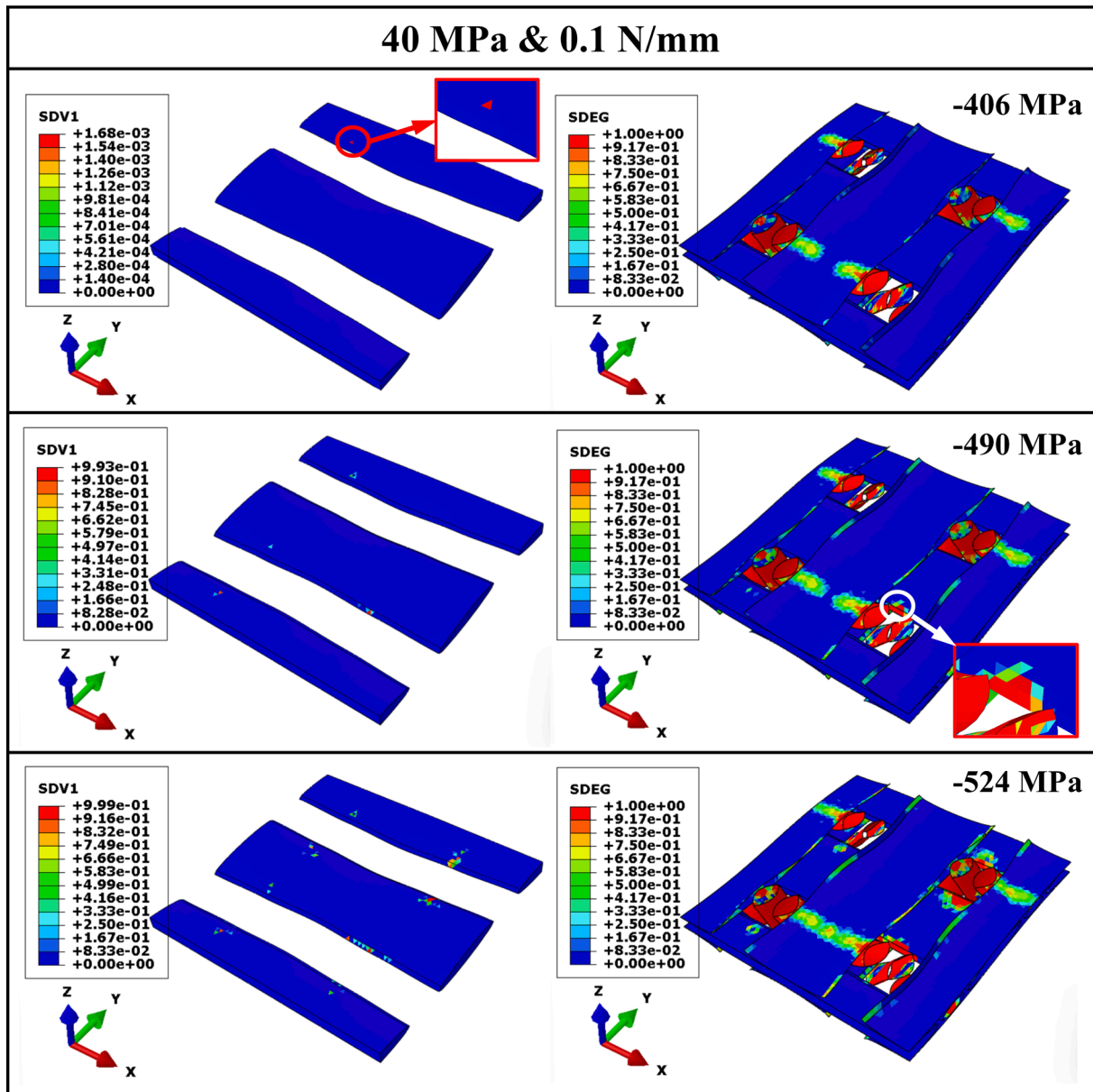
Fig. 13. Fiber kinking contours and interfacial debonding contours of 3DWC with 40 MPa interfaces under different global compressive stresses.

in Fig. 14. Due to the high-strength interface, the local stress concentration caused by the initial kinking failure of warp tows does not lead to interfacial debonding in the nearby area, making it difficult for the fiber kinking to develop further. Therefore, the damage process of 3DWC with 40 MPa interface is: first initial fiber kinking, then interfacial debonding leading to further development of fiber kinking, resulting in final failure. For the 100 MPa interface, the damage process is a gradual development of fiber kinking, unassisted by interfacial debonding. This makes the fiber kinking more difficult to develop than for the weaker interfaces. As a conclusion, when the interface strength increases, the interfacial debonding accumulates more slowly. Although both the transverse inter-fiber failure and matrix failure accumulate to some extent before the final breakage points, the kinking failure develops slowly because the warp tows have better support from surrounding components, thus the strengths of 3DWC with stronger interfaces gradually increase, until the point where no interface debonding is necessary to trigger the final failure. At this point further increase of the interfacial strength will not affect the compressive strengths.

6. Conclusion

A micromechanics-based multiscale damage model was developed to investigate the compressive failure behavior of one particular 3DWC. A *meso*-to-micro stress transfer process was established based on the SAF. With the microscopic stresses, the fiber breakage and matrix failure could be separately judged at the microscale. Using this model, the effects of interface strengths and fracture toughness on the composite compressive strength was investigated, leading to the following conclusions:

(1) A set of micromechanical analyses of micro RVC were conducted to calculate the SAF, and a parametric study was conducted to decide the numbers of key elements. It is shown that 56 matrix elements and 50 fiber elements were sufficient to capture the stress concentrations within the matrix and fiber, respectively.

(2) For the studied 3DWCs, the predicted stress–strain curves with the interfacial strength in the interval of [30, 60] MPa agreed well with the experimental curves.
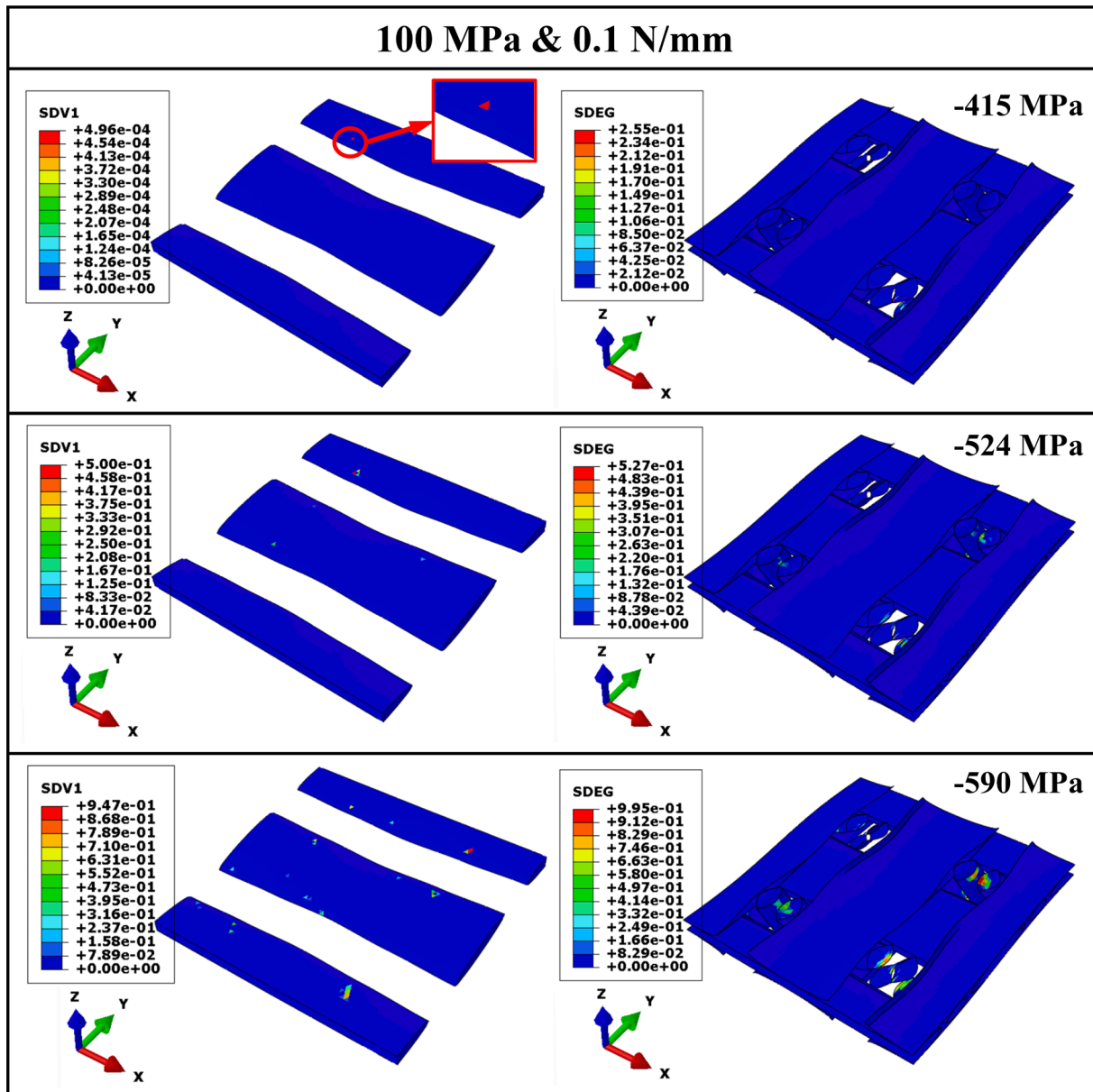
Fig. 14. Fiber kinking contours and interfacial debonding contours of 3DWC with 100 MPa interfaces under different global compressive stresses.

(3) With the increase of interface strengths and fracture toughness, the compressive resistance of the studied 3DWC is initially significantly improved, resulting in higher strength and failure strain. However, beyond a certain level further increase of the interfacial strength does not result in a corresponding increase in compressive strengths, because interfacial failure is no longer the critical failure mode.

(4) The studied 3DWCs with weak, medium and strong interfaces exhibit different damage development processes. For weak interfaces (interfacial strength 10 MPa), the damage process of 3DWC is: first interfacial debonding, then shear stress concentration, and finally fiber kinking. For medium interface (40 MPa): first initial fiber kinking, then interfacial debonding, followed by further fiber kinking leading to failure. For a strong interface (100 MPa): no interfacial debonding occurs; instead there is a progressive accumulation of fibre kinking, which is however harder to develop than for the weaker interfaces. The reason for this is that the interfacial debonding leads to a decrease in the stress transfer capacity between fiber tows and matrix, so the

kinking failure develops rapidly due to the lack of support from the surrounding components.

For developers of new composite materials, the results indicate that improvement of interfacial strength and fracture toughness can be expected to improve compressive strength initially, but will hit a point of diminishing returns as 'unassisted' fibre kinking becomes the critical damage mode. Similarly, the compressive strength of 3DWC can be classified as 'interface dominated' or 'fiber dominated' depending on the specific combination of fibres and matrix employed.

CRediT authorship contribution statement

Tao Zheng: Methodology, Investigation, Conceptualization, Formal analysis, Validation, Software, Writing – original draft. **Licheng Guo:** Supervision, Methodology, Writing – review & editing. **Ruijian Sun:** Formal analysis, Writing – review & editing. **Tongtong Wang:** Software, Writing – review & editing. **Changqing Hong:** Conceptualization, Writing – review & editing. **Rinze Benedictus:** Supervision, Writing –

review & editing. **John-Alan Pascoe:** Supervision, Conceptualization, Writing – review & editing.

Declaration of Competing Interest

The authors declare that they have no known competing financial interests or personal relationships that could have appeared to influence the work reported in this paper.

Data availability

Data will be made available on request.

Acknowledgements

References

[1] Mouritz AP, Bannister MK, Falzon PJ, Leong KH. Review of applications for advanced three-dimensional fibre textile composites. Compos Part A-Appl S 1999; 30:1445–61.

[2] Patel DK, Waas AM, Yen CF. Direct numerical simulation of 3D woven textile composites subjected to tensile loading: An experimentally validated multiscale approach. Compos Part B-Eng 2018;152:102–15.

[3] Patel DK, Waas AM, Yen CF. Compressive response of hybrid 3D woven textile composites (H3DWTCs): An experimentally validated computational model. J Mech Phys Solids 2019;122:381–405.

[4] Ullah Z, Zhou XY, Kaczmarczyk L, Archer E, McIlhagger A, Harkin-Jones E. A unified framework for the multi-scale computational homogenisation of 3D-textile composites. Compos Part B-Eng 2019;167:582–98.

[5] Patel DK, Waas AM. Damage and failure modelling of hybrid three-dimensional textile composites: a mesh objective multi-scale approach. Philos Trans Roy Soc-A 2016;374(2071):20160036.

[6] Zako M, Uetsuji Y, Kurashiki T. Finite element analysis of damaged woven fabric composite materials. Compos Sci Technol 2003;63(3-4):507–16.

[7] Zeng T, Wu L, Guo L. A finite element model for failure analysis of 3D braided composites. Mater Sci Eng A 2004;366(1):144–51.

[8] Fang G, Liang J, Wang Y, Wang B. The effect of yarn distortion on the mechanical properties of 3D four-directional braided composites. Compos Part A-Appl S 2009; 40(4):343–50.

[9] Zhang C, Xu X. Finite element analysis of 3D braided composites based on three unit-cells models. Compos Struct 2013;98:130–42.

[10] Ge J, He C, Liang J, Chen Y, Fang D. A coupled elastic-plastic damage model for the mechanical behavior of three-dimensional (3D) braided composites. Compos Sci Technol 2018;157:86–98.

[11] Hashin Z. Failure criteria for unidirectional fiber composites. J Appl Mech 1980;47: 329–34.

[12] Ha SK, Jin KK, Huang Y. Micro-mechanics of failure (MMF) for continuous fiber reinforced composites. J Compos Mater 2008;42:1873–95.

[13] Huang Y, Jin C, Ha SK. Strength prediction of triaxially loaded composites using a progressive damage model based on micromechanics of failure. J Compos Mater 2012;47(6–7):777–92.

[14] Wang L, Zheng C, Wei S, Wei Z. Micromechanics-based progressive failure analysis of carbon fiber/epoxy composite vessel under combined internal pressure and thermomechanical. Compos Part B-Eng 2016;89:77–84.

[15] Wang L, Wang B, Wei S, Hong Y, Zheng C. Prediction of long-term fatigue life of CFRP composite hydrogen storage vessel based on micromechanics of failure. Compos Part B-Eng 2016;97:274–81.

[16] Hwang YT, Choi KH, Kim JI, Lim J, Nam B, Kim HS. Prediction of non-linear mechanical behavior of shear deformed twill woven composites based on a multi-scale progressive damage model. Compos Struct 2019;224:111019.

[17] Wang M, Zhang P, Fei Q, Guo F. Modified micro-mechanics based multiscale model for progressive failure prediction of 2D twill woven composites. Chinese J Aeronaut 2020;33(7):2070–87.

[18] Zheng T, Guo L, Sun R, Li Z, Yu H. Investigation on the compressive damage mechanisms of 3D woven composites considering stochastic fiber initial misalignment. Compos Part A-Appl S 2021;143:106295.

[19] Guo J, Wen W, Zhang H, Cui H. Warp-loaded mechanical performance of 3D orthogonal layer-to-layer woven composite perforated structures with different apertures. Compos Struct 2021;278:114720.

[20] Zhang D, Liu X, Gu Y, Sun M, Yu S, Zhang Y, et al. Effects of off-axis angle on shear progressive damage of 3D woven composites with X-ray micro-computed tomography. Compos Part A-Appl S 2018;115:311–20.

[21] Huang J, Guo L, Chen L, Wang Z-X, Li J. Damage evolution of 3D woven carbon/ epoxy composites under the tension-compression fatigue loading based on multi damage information. Int J Fatigue 2022;154:106566.

[22] Zhang C, Curiel-Sosa JL, Bui T. A novel interface constitutive model for prediction of stiffness and strength in 3D braided composites. Compos Struct 2017;163:32–43.

[23] Fang G, Liang J, Wang B. Effect of interface properties on mechanical behavior of 3D four directional braided composites with large braid angle subjected to uniaxial tension. Appl Compos Mater 2011;18(5):449–65.

[24] Lu Z, Wang C, Xia B, Yang Z. Effect of interfacial properties on the uniaxial tensile behavior of three-dimensional braided composites. Comput Mater Sci 2013;79: 547–57.

[25] Lu H, Guo L, Liu G, Zhong S, Zhang L, Pan S. Progressive damage investigation of 2.5D woven composites under quasi-static tension. Acta Mechanica 2019;230(4): 1323–36.

[26] Wang R, Han J, Mao J, Hu D, Liu Xi, Guo X. A molecular dynamics based cohesive zone model for interface failure under monotonic tension of 3D four direction SiCf/ SiC composites. Compos Struct 2021;274:114397.

[27] Zhong S, Guo L, Liu G, Lu H, Zeng T. A continuum damage model for three-dimensional woven composites and finite element implementation. Compos Struct 2015;128:1–9.

[28] Li S, Wongsto A. Unit cells for micromechanical analyses of particle-reinforced composites. Mech Mater 2004;36(7):543–72.

[29] Huang Y, Jin KK, Ha SK. Effects of fiber arrangement on mechanical behavior of unidirectional composites. J Compos Mater 2008;42(18):1851–71.

[30] Jin KK, Huang Y, Lee YH, Ha SK. Distribution of micro stresses and interfacial tractions in unidirectional composites. J Compos Mater 2008;42(18):1825–49.

[31] Raghava R, Caddell RM, Yeh GSY. The macro-scopic yield behavior of polymers. J Mater Sci 1973;8:225–32.

[32] Stassi-D'Alia F. Flow and fracture of materials according to a new limiting condition of yielding. Meccanica 1967;2(3):178–95.

[33] Zheng T, Guo L, Benedictus R, Pascoe JA. Micromechanics-based multiscale progressive failure simulation of 3D woven composites under compressive loading with minimal material parameters. Compos Sci Technol 2022;219:109227.

[34] Pinho ST, Iannucci L, Robinson P. Physically based failure models and criteria for laminated fibre-reinforced composites with emphasis on fibre kinking. Part II: FE implementation. Compos Part A-Appl S 2006;37(5):766–77.

[35] Zheng T, Guo L, Huang J, Liu G. A novel mesoscopic progressive damage model for 3D angle-interlock woven composites. Compos Sci Technol 2020;185:107894.

[36] Highsmith AL, Reifsnider KL. Stiffness-reduction mechanisms in composite laminates. In: K.L. Reifsnider, Damage in Composite Materials, ASTM International. West Conshohocken; 1982. p. 103–17.

[37] Jia L, Yu L, Zhang K, Li M, Jia Y, Blackman BRK, et al. Combined modelling and experimental studies of failure in thick laminates under out-of-plane shear. Compos Part B-Eng 2016;105:8–22.

[38] Falzon BG, Apruzzese P. Numerical analysis of intralaminar failure mechanisms in composite structures. Part II: Applications Compos Struct 2011;93(2):1047–53.

[39] Fang G, Liang J, Lu Q, Wang B, Wang Y. Investigation on the compressive properties of the three dimensional four-directional braided composites. Compos Struct 2011;93(2):392–405.

[40] Needleman A. A continuum model for void nucleation by interfacial debonding. Int J Solids Struct 1987;54:525–31.

[41] Camanho PP, Davila CG. Mixed-Mode Decohesion Finite Elements for the Simulation of Delamination in Composite Materials. NASA/TM-2002-211737 2002:1–37.

[42] Vaughan TJ, McCarthy CT. Micromechanical modelling of the transverse damage behaviour in fibre reinforced composites. Compos Sci Technol 2011;71(3):388–96.

[43] de Morais AB, de Moura MF, Marques AT, de Castro PT. Mode-I interlaminar fracture of carbon/epoxy cross-ply composites. Compos Sci Technol 2002;62(5): 679–86.

[44] Li Y, Hori N, Arai M, Hu N, Liu Y, FukUnage H. Improvement of interlaminar mechanical properties of CFRP laminates using VGCF. Compos Part A-Appl S 2009; 40(12):2004–12.

[45] Qi G, Du S, Zhang B, Tang Z, Yu Y. Evaluation of carbon fiber/epoxy interfacial strength in transverse fiber bundle composite: experiment and multiscale failure modeling. Compos Sci Technol 2014;105:1–8.

[46] Sun R, Guo L, Li Z, Zhang L, Zheng T. A novel approach to assessing yarn/matrix (or yarn/yarn) in situ interfacial strength in 3D woven composites. Compos Sci Technol 2021;213:108893.